Mechanical properties of hierarchical porous silica thin films: experimental characterization by nanoindentation and Finite Element modelling

David Jauffres, Christelle Yacou, M. Verdier, Remy Dendievel, Andre Ayral

Mechanical properties of hierarchical porous silica thin films: Experimental characterization by nanoindentation and Finite Element modeling

David Jauffrès [a], Christelle Yacou [b], Marc Verdier [a], Rémy Dendievel [a,*], André Ayral [b]

[a] *Science et Ingénierie des MAtériaux et Procédés, CNRS-INPG, 1130 rue de la Piscine BP 75, F-38402 Saint Martin d'Hères Cedex, France*
[b] *Institut Européen des Membranes, CNRS-ENSCM-UM2, CC047, Université Montpellier 2, Place Eugène Bataillon, F-34095 Montpellier Cedex 5, France*

Porous thin films considered for applications like separation, sensing and microelectronic have to sustain mechanical stresses during their integration process or in working conditions. Thanks to recent progress in processing methods, it is now possible to precisely control the porosity and combine ordered mesopores with randomly-distributed macropores to achieve hierarchically porous materials. The mechanical properties of thin films containing different types of porosity (ordered meso, random macro and hierarchical) have been investigated by means of nanoindentation. In particular a method recently proposed by Li and Vlassak (H. Li, J.J. Vlassak, Journal of Materials Research 24 (2009) 1114–1126) is applied to account for the substrate effect. Residual indent impressions were imaged by Atomic Force Microscopy (AFM) to provide some insights in the mechanical behavior of the films. In addition, experimental indentation moduli are compared to theoretical predictions obtained via Finite Element (FE) analysis. The different porous structures have been modeled by FE to obtain the effective elastic properties from which the indentation modulus can be inferred. Finally, the experimental-model differences are discussed.

1. Introduction

There is a growing interest for the processing and characterization of porous thin films and membranes. These materials are considered for a large number of new applications in chemistry, biology or microelectronic. In particular porous thin films can achieve ultra low dielectric constant (κ) values required for the interlayer dielectric (ILD) material of the next generations of microprocessors, by taking advantage of the low dielectric constant of the air. Several processes, e.g. Plasma Enhanced Chemical Vapor Deposition (PECVD) or sol–gel processing, as well as several materials are considered (polymers, SiO_2, SiOCH...) [1]. However, the integration of these films reveals to be harder than expected due to several issues like the penetration of reactive gases and damage of the material during operations such as chemical mechanical polishing or packaging [2,3].

Chemistry scientists are developing ways to control precisely the porosity, providing a wide range of possibilities to act on its structure. Practically, in sol–gel processing, ordered mesoporous structures can be achieved using self-assembly surfactant molecules as porogens [4,5]. The existing large variety of surfactants gives rise to different mesostructures including periodic arrays of spherical and cylindrical pores [5]. One recent achievement on the control of the porosity is the development of so-called hierarchical porous materials based on a sol–gel processing method that combines self-assembly molecules to create an ordered mesostructure (2–50 nm) and a polymer latex to create randomly-distributed macropores (>50 nm) [4].

The prediction and characterization of porous thin-film mechanical properties are crucial to improve the processing methods and optimize the structure of the films. Mechanical characterization of very thin films is a challenging task, in particular due to the influence of the substrate. Among the different existing techniques, the Brillouin Light Scattering (BLS) [6] and laser-acoustic techniques [7,8] can probe the film only. However, the more versatile and commonly used technique is nanoindentation, also called depth-sensing indentation. This technique allows the measurement of the modulus and the hardness, and also can provide qualitative information on the mechanical behavior via microscopic imaging of the residual indent marks. However, for indentation depths superior to one-tenth of the film thickness, the influence of the substrate cannot be neglected. To account for the substrate effect in nanoindentation, several methods have been proposed recently. The easiest and more commonly used approach consists in the computation of the modulus using the classical Oliver–Pharr (OP) methodology [9,10] for several indentation depths, followed by an extrapolation to zero indentation depth. The extrapolation could be more or less sophisticated from linear [6] to exponential [7]. A semi-empirical model can also be used to fit OP results and

* Corresponding author. Tel.: +33 4 76 82 64 63.
E-mail address: remy.dendievel@simap.grenoble-inp.fr (R. Dendievel).

extrapolate the film modulus [11,12]. However, there is no real physical basis for any extrapolation function that in some cases can be ambiguous. More rigorous and elaborated approaches based on theoretical solutions have been developed by Schwarzer et al. [13] and by Li and Vlassak [14], in order to account for the substrate effect.

In terms of modeling and prediction of the mechanical properties, analytical homogenization results developed over the years for composite materials can serve as guidelines for the design of porous films [15,16]. However, for complex 3D structures, e.g. involving ellipsoidal pores due to film shrinkage, precise predictions can only be obtained by Finite Element (FE) modeling. Typically, a Representative Volume Element (RVE) is chosen for the FE computation of stresses and strains from which the stiffness matrix of the given structure can be computed. This approach was used to quantify the influence of the pore arrangement and the film shrinkage on the mechanical and dielectric properties of porous thin films [17].

To our knowledge, comparisons between FE-based theoretical prediction and experimental evaluation of the mechanical properties have rarely been conducted. Miyoshi et al. [18] compared their 2D FE model of cylindrical pores to only one nanoindentation measurement. Li et al. conducted a comparison of their nanoindentation results with FE models, but of random structures only [19]. Experimental-model confrontation is nonetheless an important step before further modeling and experimentation.

In the present paper, an experimental-FE modeling comparison of porous thin films elastic properties is presented. Firstly, porous silica thin films with different structures and densities were characterized by nano-indentation. The results were analyzed using both the Oliver–Pharr method followed by an extrapolation to zero indentation depth, and the new Li-Vlassak approach [14]. Secondly, FE modeling was conducted to get the effective stiffness matrix of the porous material, taking into account the anisotropy due to process-induced film shrinkage. Then, the indentation modulus is extracted and compared to its experimental counterpart.

2. Material

2.1. Preparation

Porous SiO_2 thin films were elaborated via the "one-pot" sol–gel technique [20]. The synthesis conditions for the SiO_2 sols were adapted from previous work by Besson [21] and Lu et al. [22]. Tetraethylorthosilicate (TEOS) was used as silica precursor, diluted in ethanol and hydrolyzed with diluted HCl (pH $\sim$ 1.25) (molar ratios TEOS: EtOH: H_2O = 1: 3.8: 5). The sol was maintained during 1 h at 60 °C under vigorous magnetic stirring. Then, porogen agents were added to create two different types of porosity (random macroporosity and ordered mesoporosity), that can be combined. Random macroporosity was generated by addition of a PolyStyrene (PS) latex (pH $\sim$ 2.3). The average particle size was determined by Scanning Electron Microscopy to be 137 nm. Triblock copolymers Pluronic® F68 ($EO_{80}PO_{30}EO_{80}$ nEO/nPO = 2.66) was used to create ordered mesoporosity ($\sim$ 4 nm). It is worth noting that the film obtained from the TEOS sol without any porogen (i.e. the matrix) already exhibits interconnected microporosity (< 2 nm) [4,23]. Five different sols were deposited by deep-coating on (100) silicon wafers to obtain the microporous matrix (Micro), two macroporous films with different porogen contents (Macro1 and Macro2), a mesoporous film (Meso) and a hierarchical film containing both macro and meso pores (Hierarch). The details of the synthesis procedures and sol composition are reported in Table 1. All the samples underwent the same thermal treatment in order to obtain the closest possible consolidation of the matrix that is highly dependant on the thermal treatment as shown by Chemin et al. [24]. The films were first exposed to a heating cycle up to 175 °C in order to consolidate the matrix. Then, the calcination of the porogens was obtained via a second heating cycle up to 450 °C.

Table 1
Sols synthesis procedures and final compositions.

Sample		Synthesis procedure	Final composition[a]
Micro	t_0	TEOS + dilute HCl (pH 1.25)	-
	t_0 + 1h30	+ Dilute HCl (pH 2.3)	
	t_0 + 2 h	Deposition	
Meso	t_0	TEOS + dilute HCl (pH 1.25)	Φ_{Vol}(F68) = 72%
	t_0 + 1 h	+ F68	
	t_0 + 1h30	+ Dilute HCl (pH 2.3)	
	t_0 + 2 h	Deposition	
Macro	t_0	TEOS + dilute HCl (pH 1.25)	Φ_{Vol}(PS) = 48% (Macro1)
	t_0 + 1h30	+ PS latex	Φ_{Vol}(PS) = 59% (Macro2)
	t_0 + 2 h	Deposition	
Hierarch	t_0	TEOS + dilute HCl (pH 1.25)	Φ_{Vol}(F68) = 72%
	t_0 + 1 h	+ F68	Φ_{Vol}(PS) = 48%
	t_0 + 1h30	+ PS latex	
	t_0 + 2 h	Deposition	

[a] In volume percentage considering only F68 and SiO_2 or PS and SiO_2.

2.2. Structural characterization

2.2.1. Film thickness

The film thicknesses were measured using a SOPRALAB spectroscopic ellipsometer. The measurements were conducted after the nanoindentation tests, allowing us to precisely probe the indented zone (the ellipsometry measure averages the thickness over a surface of 300 × 400 μm). The thickness values obtained are reported in Table 2 that summarizes the film structural characterization results.

2.2.2. Porosity

The relative contributions of the different level of porosity (micro, meso and macroporosity) were estimated from the nitrogen adsorption/desorption isotherms [23,20]. The microporosity of the matrix was evaluated to be approximately 20%. The volume fraction of micro, meso and macroporosity are reported in Table 2 for each sample.

2.2.3. Morphology

The mesoporosity (*meso* and *hierarch* samples) was characterized by means of grazing angle 2D X-ray Diffraction (2D-XRD). The diffraction pattern obtained corresponds to a Face-Centered Orthorhombic (FCO) lattice resulting from the distortion of a Body-Centered Cubic (BCC) mesophase of spherical micelles textured with the [0 1 1] axis perpendicular to the substrate [4,23] (Fig. 1). The lattice constants extracted from the pattern are a_{FCO} = 16 nm, b_{FCO} = 10 nm and c_{FCO} = 23 nm. For more details on the 2D-XRD analysis the interested reader can refer to the work done by Yacou [23] and Besson et al. [25].

Table 2
Structural characterization of the porous silica films.

Sample	Film thickness (nm)	Pore volume fraction			Structure
		Micro	Meso	Macro	
Micro	279 ± 2	0.20	0	0	–
Meso	593 ± 2	0.10	0.50	0	FCO
Macro1	267 ± 2	0.12	0	0.39	Random
Macro2	278 ± 2	0.10	0	0.50	Random
Hierarch	548 ± 2	0.08	0.38	0.24	FCO + Random

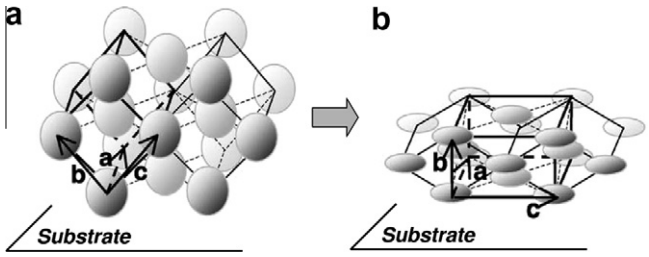

Fig. 1. (a) Initial BCC lattice with (0 1 1) parallel to the substrate. (b) FCO lattice of the film after drying and shrinkage. (0 1 0) is aligned with the substrate.

The FCO lattice constants identified correspond to a shrinkage ε = 56% of the initial BCC structure in the direction perpendicular to the substrate. The shrinkage is assumed to occur without deformation in the directions parallel to the substrate (i.e. a_{BCC} = $a_{FCO=}$ 16 nm), in accordance with previous reports on this type of thin films [23,26]. Scanning Electron Microscope (SEM) and Transmission Electron Microscope (TEM) observations of the *hierarch* sample confirm the presence of both ordered mesopores and randomly-distributed macropores (Fig. 2). The images also provide the size and shape of the macropores that reveal to be oblate ellipsoids of approximately 50 nm × 100 nm, which corresponds to 50% shrinkage. This value is consistent with the mesostructure lattice shrinkage (56%).

3. Experimental

3.1. Methods

3.1.1. Nanoindentation measurements

Nanoindentation tests were conducted on a MTS Nanoindenter DCM machine equipped with a diamond Berkovitch tip. The Constant Stiffness Measuring (CSM) mode was used to apply an oscillating load. The frequency of the oscillation was 75 Hz and the amplitude 1 nm. Between four and six independent measurements were done on each film and averaged. The residual indent marks were observed on a NanoscopeIII Di AFM in standard tapping mode. The classical Oliver–Pharr analysis [9,10] is described first, and then the Li-Vlassak approach [14] used to account for the substrate effect is presented.

3.1.2. Oliver–Pharr (OP) analysis

The classical OP methodology is based on the elastic nature of the unloading. Under this assumption, the hardness H and the indentation modulus M can be computed from the load–displacement P-h indentation curve (Fig. 3a) as follow [9,10]:

$$H = \frac{P_{max}}{A} \tag{1}$$

$$M = \frac{S\sqrt{\pi}}{2\beta\sqrt{A}} \tag{2}$$

P_{max} is the maximum load, S = dP/dh the elastic unloading stiffness, A the contact area and β a correction factor equal to 1.034 for a Berkovitch indenter. The contact area is obtained from the contact depth h_c and the tip area function f calibrated by measurements on fused silica (Fig. 3b):

$$h_c = h_{max} - \varepsilon\frac{P}{S} \tag{3}$$

$$A = f(h_c) \tag{4}$$

h_{max} is the maximum displacement and ε a constant equal to 0.75 for a Berkovitch indenter.

The CSM mode allows the continuous computation of the contact stiffness S from the dynamic response of the system [27] which permits the computation of both M and H as a function of the indentation depth. When testing soft film on hard substrate system, M and H increase with h as a consequence of increasing substrate influence (Fig. 4). One could thus extrapolate the results to zero indentation depth in order to remove the substrate effect.

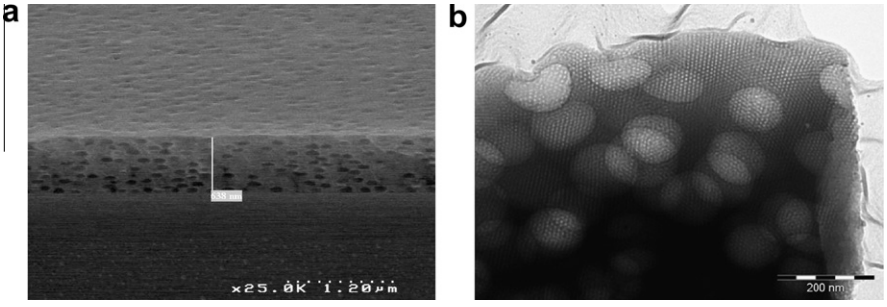

Fig. 2. Silica film with hierarchical porosity. (a) Edge-on view showing oblate macropores (SEM) and (b) TEM showing macro and mesopores.

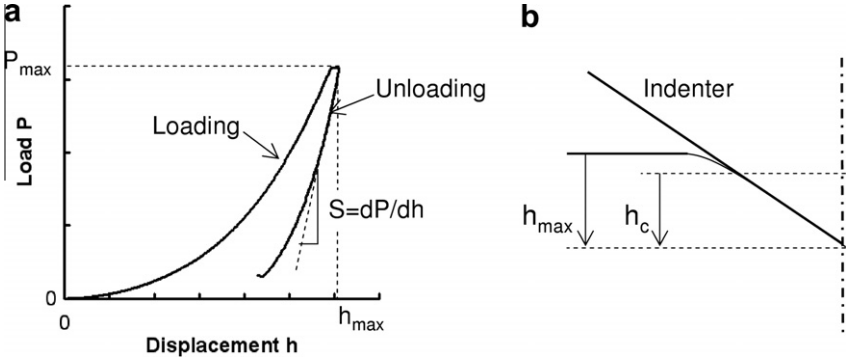

Fig. 3. (a) Typical load–displacement indentation curve (b) Contact geometry.

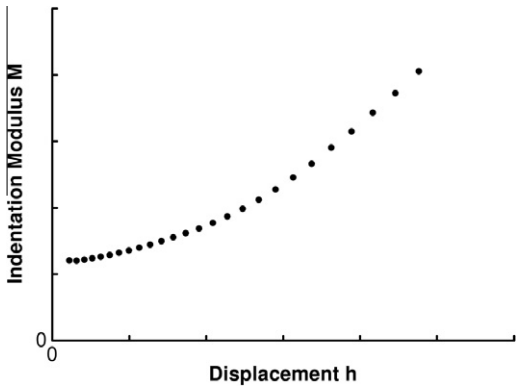

Fig. 4. Typical indentation modulus versus displacement curve obtained via CSM measurement mode.

Linear extrapolation [6] with limited amount of data points or exponential extrapolation [7,12] are generally used.

3.1.3. Li-Vlassak (LV) analysis

The method recently proposed by Li and Vlassak [14] was also used to account for the influence of the substrate. This method allows the computation of the film-only indentation modulus M_f, decorrelated from the substrate influence, while the OP method compute only the global indentation modulus M that needs to be extrapolated.

Li and Vlassak have shown that for an elastic contact the relationship between S and $a = \sqrt{A/\pi}$ the contact radius is independent of the precise indenter shape and can be theoretically calculated for a given film/substrate system using Yu's analytical work [14,29]. In addition, for an elasto-plastic indentation, the unloading from a hardness impression can be assimilated to an elastic contact between a flat surface and an "effective" indenter shape, thus allowing the fitting of the experimental and theoretical relationships between S and a.

However, the numerical resolution of Yu's solution [28] is time-consuming and the complete fitting procedure can take several hours on a conventional personal computer. It appears to us more advantageous to instead use the closed-form solution for a spherical indenter published by Hsueh and Miranda [29]. This solution, established using a combined empirical-analytical method, shows no noticeable difference from Yu's solution when considering the S-a relation for soft film on hard substrate.

The LV procedure thus consists in an iterative fitting of two parameters, M_f and η to match the experimental and theoretical S-a curves. η is a parameter that quantifies the local thinning of the film due to non-elastic deformation and allows the determination of an "effective" thickness t_{eff} that will be used in the computation of the theoretical S-a relationship:

$$t_{eff} = t - \eta h \tag{5}$$

t is the film thickness and h the indentation depth.

The method begins by assuming initial values for M_f and η to calculate the corresponding experimental contact radius a_{exp}. The computation of a_{exp} follows OP with the addition of a correction factor ξ to account for the substrate effect, and is given by the following implicit equation:

$$a_{exp} = \sqrt{\frac{1}{\pi} f(h - \xi(a_{exp}, M_f, \eta)\varepsilon \frac{P}{S})} \tag{6}$$

ξ is obtained from Hsueh and Miranda solution for a spherical indenter having a radius to film thickness ratio R/t equal to 30. The difference with ξ computed for a conical indenter using Yu's solution is small and the a_{exp} value is nearly unaffected by this approximation. To remove the indenter tip compliance, the reduced stiffness S_r is calculated using a_{exp}:

$$S_r = (\frac{1}{S} - \frac{1}{S_{tip}})^{-1} \tag{7}$$

$$S_{tip} = 2a_{exp}\frac{E_{tip}}{1 - \nu_{tip}^2} \tag{8}$$

E_{tip} and ν_{tip} are the Young's modulus and the Poisson ratio of the indenter.

Then, the theoretical S-a relationship is computed from the data of the problem, i.e. t_{eff}, M_f and the elastic properties of the substrate, using the closed-form solution established by Hsueh and Miranda [29]. The theoretical contact radii a_{theo} corresponding to each experimental value S_r are deduced from this theoretical S-a relation and finally a standard optimization algorithm is used to find M_f and η that minimize the following objective function:

$$\chi^2 = \sum (a_{exp} - a_{theo})^2 \tag{9}$$

The anisotropic substrate ((100) silicon wafer) was approximated by an isotropic material with a Young's modulus equal to 160 GPa (value for polycrystalline silicon [30]). Hsueh and Miranda closed-form solution is only available for film and substrate with Poisson ratios of 0.25, i.e. slightly higher than the SiO_2 (~0.17 [31]) and Poly-Si (~0.22 [30]) values. However, Poisson ratios of the film and of the substrate have little influence both on ξ and on the results of the fit as shown by Li and Vlassak [14].

In addition to removing the ambiguity of the extrapolation of OP results, the LV approach also provide the consideration of:

- the influence of the film on the calculation of the contact depth through the correction factor ξ,
- the effective thinning of the film through the parameter η.

3.2. Results

3.2.1. Oliver–Pharr

Fig. 5 provides the indentation moduli computed using the OP method. Due to the extremely low thickness of the films, the substrate influence is significant and the modulus increases rapidly and in a non-linear manner above a normalized indentation depth of 0.2. In addition, for indentation depths lower than around 50 nm the dispersion increases, in particular for the films with macropores. The particularly high roughness due to the existence of macropores near the surface likely causes this significant dispersion, as well as the lack of representativity of the probed volume due to heterogeneity at this lengthscale. The usable data points for a linear extrapolation to zero indentation depth are thus limited. It was chosen to perform the extrapolation of the first four linearly aligned data points (Fig. 5 and Table 3). This procedure ensures that the first points are not used and that the extrapolation is not influenced by the non-linearity appearing at high h/t, which is confirmed by excellent determination coefficients (Table 3). The uncertainty given in Table 3 corresponds to the average standard deviation observed on the data points used for the extrapolation.

3.2.2. Li-Vlassak

The LV approach was used to analyze the nanoindentation data in order to account more rigorously for the substrate effect. The LV method is based on a fit to a theoretical solution of the film/substrate indentation and thus allows the use of all the data points at high indentation depth. With the advantage of being able to use large depth data points, it is possible to exclude the points with

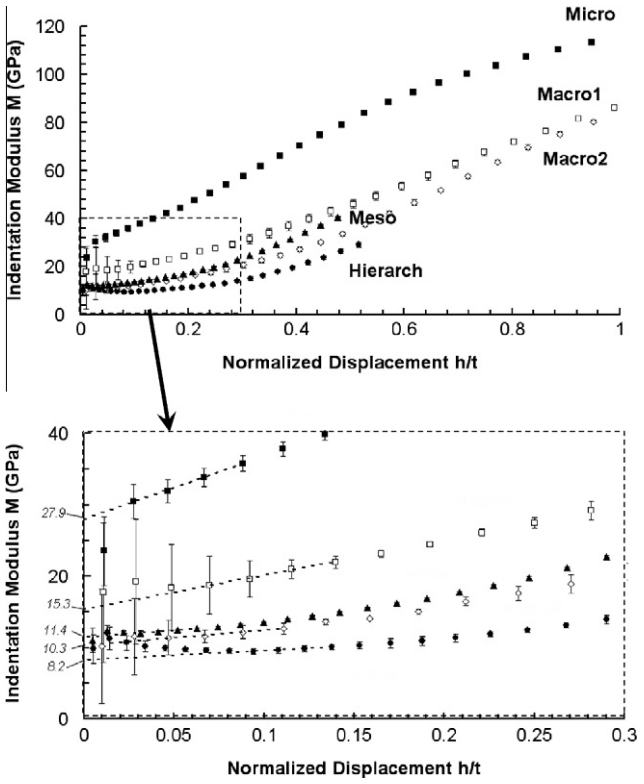

Fig. 5. Indentation modulus vs normalized displacement h/t and linear extrapolation to zero indentation depth. (■) *Micro* (□) *Macro1* (▲) *Meso* (◇) *Macro2* (●) *Hierarch*.

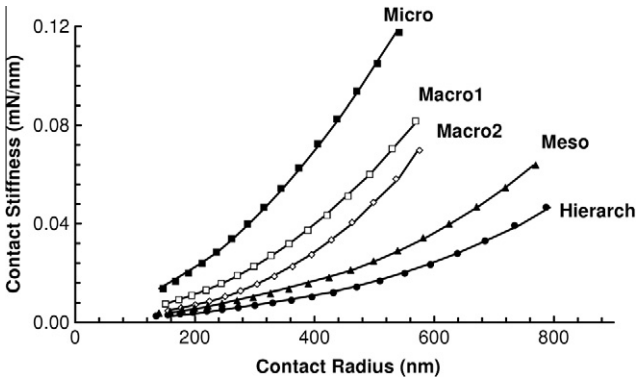

Fig. 6. Contact stiffness S versus contact radius. Markers: experimental data points. Solid lines: fit using LV.

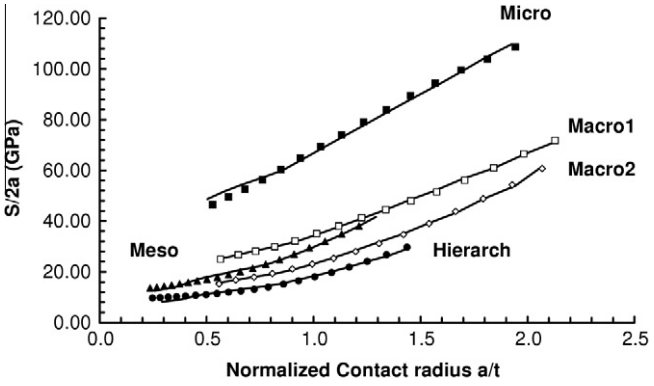

Fig. 7. S/2a versus a/t. Markers: experimental data points. Solid lines: fit using LV.

Table 3
Nanoindentation results.

Sample	OP linear extrapolation		LV fit	
	M_f (GPa)	R^2	M_f (GPa)	η
Micro	27.9 ± 1.6	0.998	30.7 ± 0.5	0.76
Meso	11.4 ± 0.4	0.997	10.0 ± 0.1	0.97
Macro1	15.3 ± 2.2	0.995	14.2 ± 0.7	0.57
Macro2	10.3 ± 1.2	0.965	8.5 ± 0.4	0.78
Hierarch	8.2 ± 0.2	0.999	6.3 ± 0.2	0.81

indentation depths inferior to 50 nm that exhibit large uncertainties. In addition, at low indentation depth the behavior is purely elastic during loading, which causes the experimental contact radius to be improperly evaluated [14]. The data used for the fit have also been limited at the other end to $h/t = 2/3$ to avoid delamination or cracking of the film to influence the analysis [14]. As observed in Fig. 6 and 7 the quality of the fit is very good over all the data points used. The corresponding LV parameters, M_f and η are reported in Table 3. Note that LV gives lower indentation moduli than OP for all the films except for the *micro* one and that the differences between the two methods are reasonable, ranging from 6 to 23%.

3.2.3. AFM observations

The indent marks have been observed by AFM in order to investigate the deformation behavior of the films and to validate the approach used to estimate the contact area (Eq. (6)) within the LV method. The AFM height images and the profiles of the residual indent impressions are provided in Fig. 8 for the *micro* and *meso* films and in Fig. 9 for the *macro2* and *hierarch* films. Note that because the film thicknesses are different ($\sim$ 600 nm for *meso* and *hierarch* versus $\sim$300 nm for the rest of the samples), AFM height images of 300 nm depth indents are reported for *meso* and *hierarch*, and 200 nm depth indents for *micro* and *macro2* in order to compare indents with similar h/t values.

Firstly, in order to check the methodology used to estimate the contact areas (risks of underestimation in case of pile-up [32]), these latter have been measured on the AFM images and compared with the areas estimated from Eq. (6). The threshold technique used to measure the areas was not applicable to *macro* and *hierarch* samples because of the significant roughness of their surface. As observed in Fig. 10, an acceptable agreement with the values estimated by Eq. (6) is observed, thus validating the approach used to estimate the contact areas.

Secondly, the film mechanical behaviors have been analyzed in light of the AFM images. It is observed in Figs. 8 and 9 that each sample exhibits a markedly different behavior:

- the *micro* film is characterized by a little pile-up and a limited elastic recovery (final indentation depth/maximum indentation depth $h_f/h_{max} \sim 0.85$),
- the *meso* film shows a sink-in and a significant elastic recovery ($h_f/h_{max} \sim 0.55$),
- the *macro2* film shows no elastic recovery and a completely pyramidal indent impression with plane facets,
- the *hierarch* has a behavior similar to the *macro2* sample but with a little elastic recovery ($h_f/h_{max} \sim 0.9$).

The *micro* and *meso* films have a typical elasto-plastic behavior while the *macro* and *hierarch* films have a typical rigid-plastic

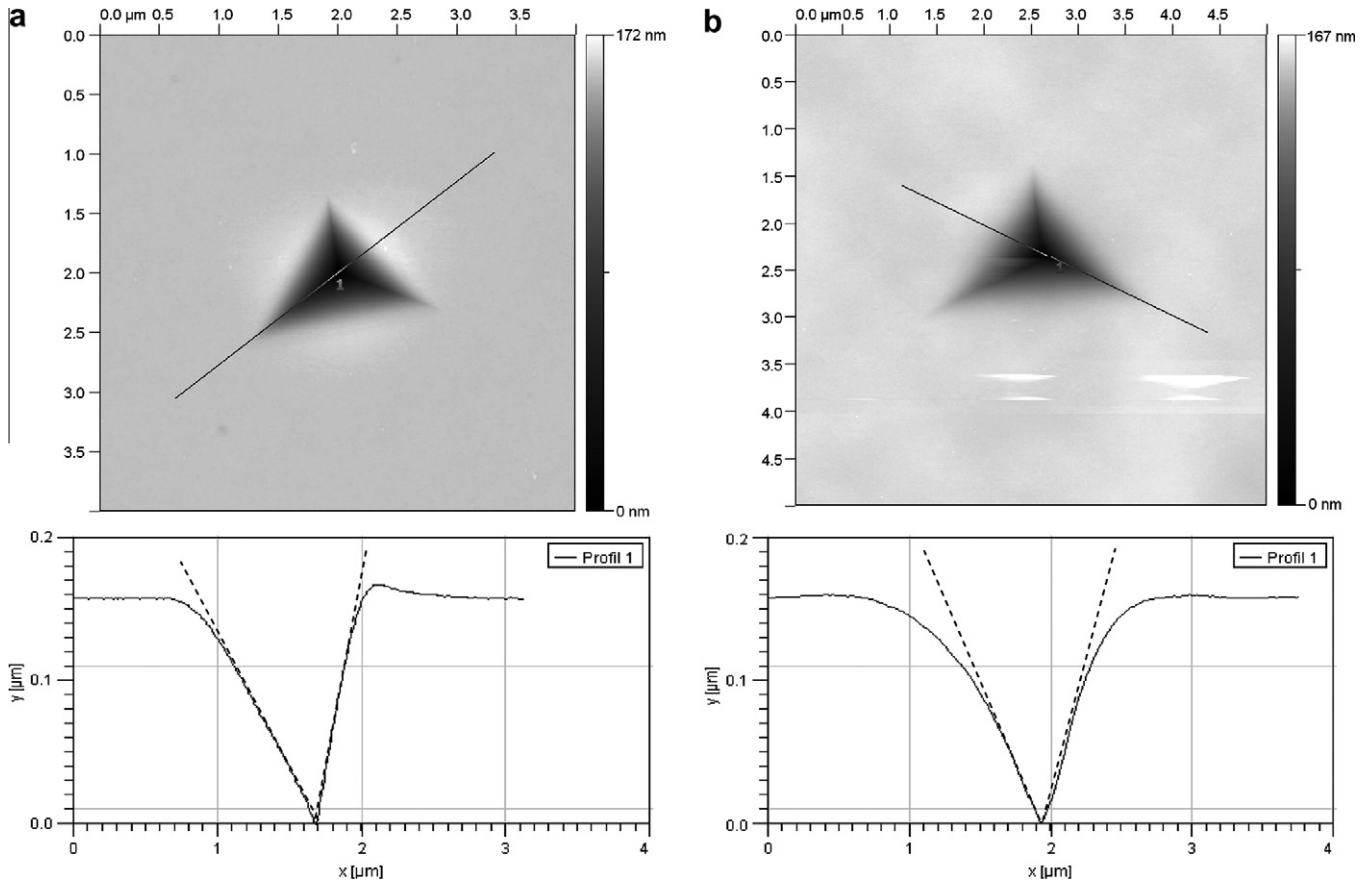

Fig. 8. AFM observation of (a) *micro* / 200 nm depth indentation (b) *meso* / 300 nm depth indentation. Straight dash lines serve to accentuate the profile.

behavior [32]. It is believed that this rigid-plastic appearance is a consequence of an irreversible deformation by brittle collapse of the macropores [33]. Indeed, this deformation mode forbids any elastic recovery during unloading. The *meso* sample has a behavior typical of an elasto-plastic material with a low Young's modulus/yield stress (E/σ_y) ratio while the *micro* sample behavior is typical of a higher E/σ_y ratio [9,32].

It is worth noting that while being highly porous, the *meso* film does not seem to have a brittle behavior, in opposition to the samples with macropores. These deformation behavior differences are probably the cause of the notably different hardness behaviors observed in Fig. 11: after an initial increase, *macro* and *hierarch* samples exhibit a decrease in hardness followed by a plateau while *micro* and *meso* samples show a constantly-increasing hardness consistent with a substrate effect. One interpretation could be that after a short initial elasto-plastic behavior leading to hardness $H \sim 3\sigma_y$ [34], the brittle pore collapse proceeds within samples containing macroporosity. During the brittle collapse $H \sim \sigma_{cs} \sim \sigma_y$ (σ_{cs} being the film compressive strength) [35], which explains the hardness decrease. In addition, in case of a brittle pore collapse under the indenter, the elasto-plastic field will be smaller which limits the substrate influence compared to a plastic material.

4. Modeling

COMSOL mutliphysics FE software was used to perform the simulations. The two structures encountered in the films studied, i.e. pores ordered on a FCO lattice and pores randomly distributed, were modeled by FE using the concepts of Repeating Unit Cell (RUC) and Representative Volume Element (RVE) [17,36]. The whole density range was studied for both structures and the effective elastic constants were computed from average strains and stresses. The underlying hypothesis of the FE computation of the effective mechanical properties is that the matrix properties are constant. It is important to remind here that the solid mechanics concepts, in particular the elasticity theory used in the present FE modeling, are applicable as long as the matrix material can be assumed homogeneous, i.e. down to the scale where molecular and atomic heterogeneities do not have to be considered. Consequently, only the influence of the structure (pores shape and arrangement) is taken into account, regardless of the scale considered.

4.1. Geometry and boundary conditions

The modeling is done on a RUC for the ordered mesostructure and on a RVE for the randomly-distributed macropores. Periodic Boundary Conditions (BC) [37] were used for all the computations.

The ordered structure RUC was created based on the FCO lattice constants determined by 2D-XRD (see 2.2). The unit cell is a parallelepiped of dimensions $a \times a\sqrt{2} \times a\sqrt{2}$. The pores are oblate ellipsoids resulting from shrinkage of 56% perpendicular to the substrate.

Random sequential addition process was used to generate random closed-spherical-pore structures up to the pore volume fraction limit reachable using this method, i.e. 0.38 [15]. Higher pore volume fractions were obtained using the dp3D discrete element simulation software [38]. This code can generate random

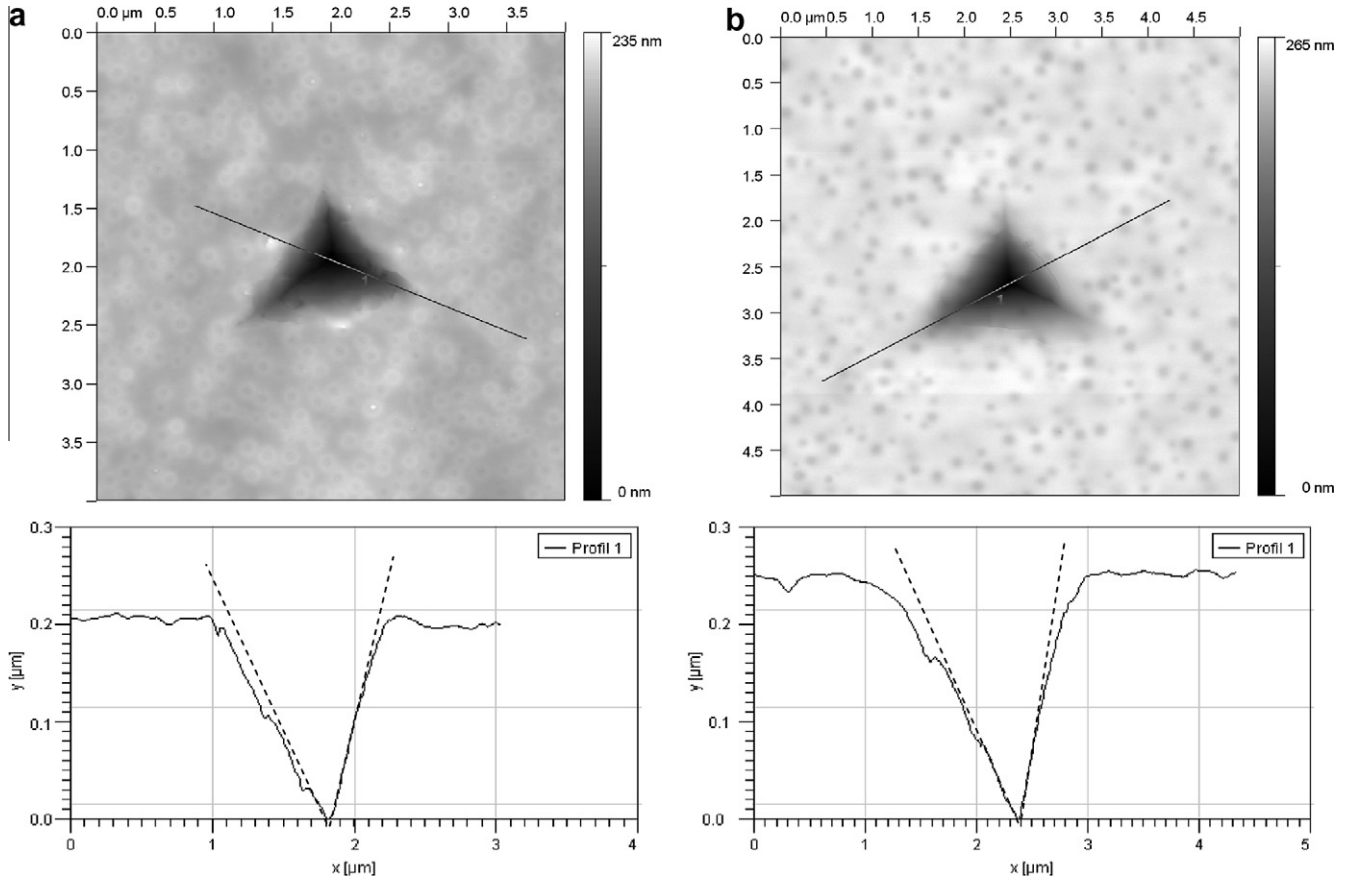

Fig. 9. AFM observation of (a) *macro2* / 200 nm depth indentation (b) *hierarch* / 300 nm depth indentation. Straight dash lines serve to accentuate the profile.

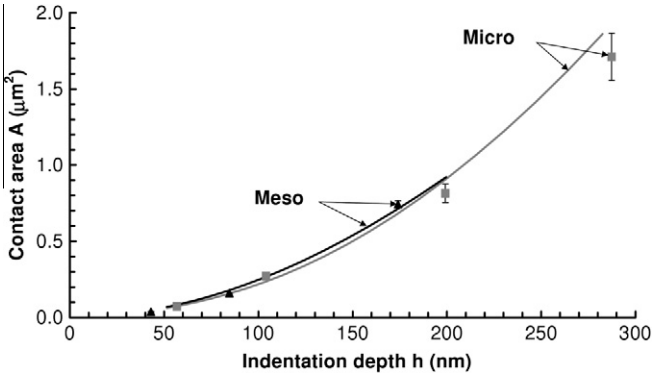

Fig. 10. AFM and LV contact areas. Plain lines: contact areas estimated by LV (Eq. (6)). Symbols: contact areas measured on AFM images.

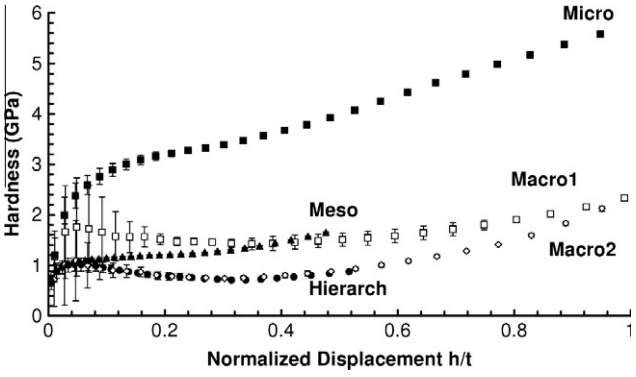

Fig. 11. Hardness vs normalized displacement h/t. (■) *Micro* (□) *Macro1* (▲) *Meso* (◇) *Macro2* (●) *Hierarch*.

spheres in equilibrium by densification of an initial distribution obtained by RSA, using contact laws. Very high sphere stiffness was chosen and the sphere radius was reduced by 2% before the meshing step in order to avoid getting contacting pores. The actual pore structures after shrinkage (50% as deduced from TEM/SEM imaging) were obtained by homothetic transformation of these initial structures. The geometries are then free-meshed with quadratic tetrahedral elements (Fig. 12). In order to have a valid RVE, the ratio pore radius/side of the volume was kept inferior or equal to 0.15. The validity of the RVE was checked by computing the Young's modulus for three different structures with the same density. The relative standard deviation between the three computations was kept below 2% using periodic BC, which validates the RVE.

4.2. Simulation and homogenization

The effective compliance matrix [S] is determined assuming an orthotropic symmetry. Under this hypothesis the Hooke's law takes the following form using Voigt notation for [S] [15]:

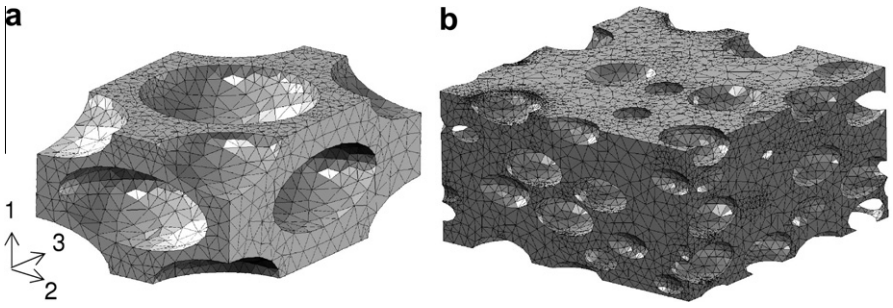

Fig. 12. Meshes of (a) RUC of the FCO pore structure and (b) RVE of the randomly-distributed pore structure.

$$\begin{bmatrix} \overline{\varepsilon}_{11} \\ \overline{\varepsilon}_{22} \\ \overline{\varepsilon}_{33} \\ 2\overline{\varepsilon}_{23} \\ 2\overline{\varepsilon}_{13} \\ 2\overline{\varepsilon}_{12} \end{bmatrix} = \begin{bmatrix} S_{11} & S_{12} & S_{13} & 0 & 0 & 0 \\ S_{12} & S_{22} & S_{23} & 0 & 0 & 0 \\ S_{13} & S_{23} & S_{33} & 0 & 0 & 0 \\ 0 & 0 & 0 & S_{44} & 0 & 0 \\ 0 & 0 & 0 & 0 & S_{55} & 0 \\ 0 & 0 & 0 & 0 & 0 & S_{66} \end{bmatrix} \cdot \begin{bmatrix} \overline{\sigma}_{11} \\ \overline{\sigma}_{22} \\ \overline{\sigma}_{33} \\ \overline{\sigma}_{23} \\ \overline{\sigma}_{13} \\ \overline{\sigma}_{12} \end{bmatrix} \tag{10}$$

$\overline{\varepsilon}_{ij}$ and $\overline{\sigma}_{ij}$ are the average strains and stresses.

Uniaxial compressions in the directions 1, 2 and 3 are successively applied to the RUC/RVE (state of strain I, II, and III, respectively). The corresponding average stresses $(\bar{\sigma}_{ij})_I$, $(\bar{\sigma}_{ij})_{II}$ and $(\bar{\sigma}_{ij})_{III}$ are obtained by integration of the FE results, and a system of 6 equations can be built from the Hooke's law to compute S_{11}, S_{22}, S_{33}, S_{12}, S_{13} and S_{23}:

$$\begin{bmatrix} (\overline{\sigma}_{11})_I & 0 & 0 & (\overline{\sigma}_{22})_I & (\overline{\sigma}_{33})_I & 0 \\ 0 & (\overline{\sigma}_{22})_I & (\overline{\sigma}_{33})_I & (\overline{\sigma}_{11})_I & (\overline{\sigma}_{11})_I & (\overline{\sigma}_{22})_I + (\overline{\sigma}_{33})_I \\ 0 & (\overline{\sigma}_{22})_{II} & 0 & (\overline{\sigma}_{11})_{II} & 0 & (\overline{\sigma}_{33})_{II} \\ (\overline{\sigma}_{11})_{II} & 0 & (\overline{\sigma}_{33})_{II} & (\overline{\sigma}_{22})_{II} & (\overline{\sigma}_{11})_{II} + (\overline{\sigma}_{33})_{II} & (\overline{\sigma}_{22})_{II} \\ 0 & 0 & (\overline{\sigma}_{33})_{III} & 0 & (\overline{\sigma}_{11})_{III} & (\overline{\sigma}_{22})_{III} \\ (\overline{\sigma}_{11})_{III} & (\overline{\sigma}_{22})_{III} & 0 & (\overline{\sigma}_{11})_{III} + (\overline{\sigma}_{22})_{III} & (\overline{\sigma}_{33})_{III} & (\overline{\sigma}_{33})_{III} \end{bmatrix} \cdot \begin{bmatrix} S_{11} \\ S_{22} \\ S_{33} \\ S_{12} \\ S_{13} \\ S_{23} \end{bmatrix} = \begin{bmatrix} (\overline{\varepsilon}_{11})_I \\ 0 \\ (\overline{\varepsilon}_{22})_{II} \\ 0 \\ (\overline{\varepsilon}_{33})_{III} \\ 0 \end{bmatrix} \tag{11}$$

S_{44}, S_{55} and S_{66} are obtained from pure shear simulations in the 23, 13 and 12 planes:

$$S_{44} = \frac{2\overline{\varepsilon}_{23}}{\overline{\sigma}_{23}}; \quad S_{55} = \frac{2\overline{\varepsilon}_{13}}{\overline{\sigma}_{13}}; \quad S_{66} = \frac{2\overline{\varepsilon}_{12}}{\overline{\sigma}_{12}}. \tag{12}$$

The typical value of the Poisson ratio for SiO_2, 0.17, is used [31]. More details on the modeling aspects can be found in a dedicated article [17].

4.3. Indentation modulus

For an isotropic material, the indentation modulus is a function of the Young modulus E and the Poisson ratioν [9,10].

$$M = \frac{E}{1 - \nu^2} \tag{13}$$

The case of an orthotropic material is more complex and M will be a weighted average of all the stiffness constants, albeit with more weight for the indentation direction. Delafargue et al. have proposed the following approximate closed-form relationships to calculate the indentation modulus M_1 in the direction *x1*, (*x1*,*x2*), (*x1*,*x3*) and (*x2*,*x3*) being the three planes of symmetry of the orthotropic material [39]:

$$M_1 \approx \sqrt{M_{13} M_{12}} \tag{14}$$

$$M_{13} = 2\sqrt{\frac{C_{31}^2 - C_{13}^2}{C_{33}} \left(\frac{1}{C_{55}} + \frac{2}{C_{31} + C_{13}}\right)^{-1}} \tag{15}$$

$$M_{12} = 2\sqrt{\frac{C_{21}^2 - C_{12}^2}{C_{22}} \left(\frac{1}{C_{66}} + \frac{2}{C_{21} + C_{12}}\right)^{-1}} \tag{16}$$

with $C_{31} = \sqrt{C_{11} C_{33}}$ and $C_{21} = \sqrt{C_{11} C_{22}}$

C_{ij} are the stiffness matrix ($[C] = [S]^{-1}$) components in Voigt notation.

5. Experimental-model comparison and discussion

The normalized indentation moduli deduced from the FE analyses are reported in Fig. 13 with the experimental data obtained by the OP and LV methods. The experimental indentation moduli were normalized by the matrix indentation modulus (*micro* sample)

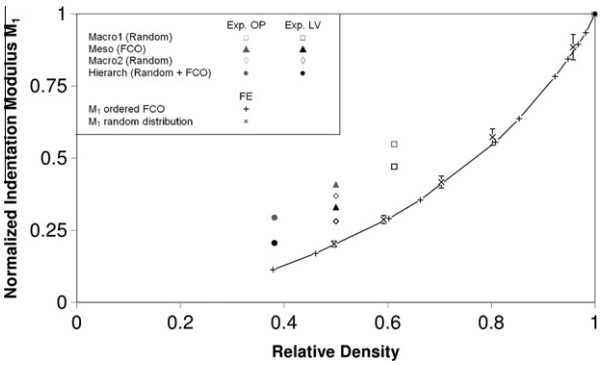

Fig. 13. Normalized indentation modulus M_1 vs relative density. Reference for the normalization and relative density is the microporous matrix. Experimental – FEA comparison.

obtained with the same method (OP or LV). To stay consistent, the density reported in Fig. 13 is thus the relative density to the matrix and not to dense SiO_2. This normalization by the matrix properties is more appropriate than by dense SiO_2 as an incomplete crosslinking is expected from sol–gel processing, thus leading to walls with properties deviating from dense SiO_2. Precautions in sample preparation were taken to ensure as much as possible that the SiO_2 microporous matrix is similar for all the samples. However, differences in matrix properties between the samples cannot be completely ruled out, in particular because of the use of different types of porogens.

In accordance with an extended FE element study of thin film porous structures [17], the theoretical elastic responses of FCO and random pore structures are similar.

Concerning the experimental results, more confidence is placed in LV results, because the extrapolation of OP results could be ambiguous. Indeed, in addition to uncertainties due to the use of low indentation depth data points, the extrapolation uses a very limited number of points.

In both cases, the experimental values are superior to the theoretical ones, which suggests that the films could exhibit significant densification under the indenter which would cause an overestimation of their modulus [40–42]. Note that Chen et al. [40] concluded that densification has a minor influence because the densified zone stays small compared to the zone elastically deformed, but their study relates to ductile porous materials with porosity inferior to 0.3. We believe that it is no more the case for higher porosities, in particular if the material exhibits brittle pore collapse. Indeed, if deformation occurs by brittle collapse, the zone deformed is reduced compared to an elasto-plastic field, thus increasing the influence of the densified zone. LV method does not account for such an indentation effect, the film indentation modulus being assumed constant. One way to include this effect in the analysis of the indentation data would be to use an FE-based inverse method with a constitutive law accounting for densification under a hydrostatic pressure.

For the *meso* and *hierarch* films, a nanoconfinement effect could superimpose and also increase the indentation modulus by increasing the matrix modulus. Indeed, in thin silica walls, an increase in the concentration of small siloxane rings (three and four-membered rings) can lead to a significant increase of the modulus. FCO lattice constants and density of the *meso* film correspond to wall thicknesses as thin as 1 to 2 nm which is compatible with the apparition of this nanoconfinement effect [43]. It would explain the nearly 20% higher indentation modulus measured on the *meso* film compared to the *macro2* film, while they have the same density and the FE models do not show any differences between the two structures.

On a practical point of view, interesting conclusions can be deduced from this study. First, the introduction of macroporosity in a mesoporous film allows the achievement of a highly porous film (62% of porosity) but leads to a brittle behavior that may be unacceptable for some applications. In addition, at a given porosity, the ordered mesoporous structure exhibits a higher modulus than the macroporous structure that could originate in a nanoconfinement effect in thin silica walls. Consequently, ordered mesoporosity turns out to be a better choice than random macroporosity as it combines a more ductile behavior and a higher stiffness.

6. Conclusion

Mesoporous, macroporous and hierarchically porous thin films were investigated by means of nanoindentation. The mesoporosity is ordered on a FCO lattice while the macropores are randomly distributed. The films were very thin and special attention was given to account for the substrate effect. Two different approaches were used to obtain the indentation moduli of the films only:

- the extrapolation to zero indentation depth of the moduli obtained by the Oliver–Pharr analysis for different indentation depths,
- the use of a recent method proposed Li and Vlassak [14].

More confidence is placed on the results obtained via the LV method that is based on a fit to the theoretical S-a plot while the first approach is only an empirical extrapolation.

The analysis of the mechanical behavior of the films, by AFM imaging of the residual indent marks, shows that the macroporous and hierarchically porous films have a specific behavior, characterized by a very short elastic deformation followed by the brittle collapse of the macropores. Interestingly, the mesoporous film has a completely opposite behavior with a classical elasto-plastic behavior and a significant elastic recovery.

The theoretical indentation modulus was computed for each film from FE analysis based on the actual film porous structures. Even accounting rigorously for the substrate effect with the LV method, the experimental indentation moduli are superior to the theoretical ones, which suggests that other phenomena influence the indentation. A first phenomenon could be the material densification under the indenter that would lead to an overestimation of the modulus. For the mesoporous and hierarchically porous films, another effect could superimpose: the increase of the matrix modulus by nanoconfinement effect in silica walls inferior to 2 nm. On a practical point of view, the ordered mesoporous structure turns out to be a better choice than the random macroporous one as it exhibits a higher modulus combined with a more ductile behavior.

Acknowledgements

The authors would like to acknowledge J-L Sthele (SOPRALAB), P-A Albouy (LPS), L. Datas (CIRIMAT), D. Cot and A. El Mansouri (IEM) for the ellipsometry, XRD, TEM, SEM and N_2 adsorption measurements, respectively. This work was supported by the French National Research Agency (ANR) in the scope of the program PICSSEL.

References

[1] W. Volksen, R.D. Miller, G. Dubois, Chem. Rev. 110 (2009) 56–110.
[2] P. Leduc, M. Savoye, S. Maitrejean, D. Scevola, V. Jousseaume, G. Passemard, Proceedings of the International Interconnection Technology Conference, Burlingame, USA, 2005.
[3] T.S. Kim, R.H. Dauskardt, IEEE Trans. Device Mater. Reliab. 9 (2009) 509–515.
[4] C. Yacou, A. Ayral, A. Giroir-Fendler, M. Fontaine, A. Julbe, Microporous Mesoporous Mater. 126 (2009) 222–227.
[5] V.V. Guliants, M.A. Carreon, Y.S. Lin, J. Membr. Sci. 235 (2004) 53–72.
[6] N. Chérault, G. Carlotti, N. Casanova, P. Gergaud, C. Goldberg, O. Thomas, M. Verdier, Microelectronic Engineering 82 (2005) 368–373.
[7] M. Herrmann, N. Schwarzer, F. Richter, S. Frühauf, S. Schulz, Surf. Coat. Technol. 201 (2006) 4305–4310.
[8] D. Schneider, T. Witke, T. Schwarz, B. Schöneich, B. Schultrich, Surf. Coat. Technol. 126 (2000) 136–141.
[9] W.C. Oliver, G.M. Pharr, J. Mater. Res. 19 (2004) 3–20.
[10] W.C. Oliver, G.M. Pharr, J. Mater. Res. 7 (1992) 1564–1583.
[11] R. Saha, W.D. Nix, Acta Mater. 50 (2002) 23–38.
[12] L. Wang, M. Ganor, S.I. Rokhlin, J. Mater. Res. 20 (2005) 2080–2093.
[13] T. Chudoba, N. Schwarzer, F. Richter, Surf. Coat. Technol. 127 (2000) 9–17.
[14] H. Li, J.J. Vlassak, J. Mater. Res. 24 (2009) 1114–1126.
[15] S. Torquato, Random Heterogeneous Materials, New-York, Springer-Verlag, 2002.
[16] S. Torquato, A. Donev, A.G. Evans, C.J. Brinker, J. Appl. Phys. 97 (2005) 124103.
[17] D. Jauffres, R. Dendievel, M. Verdier, Microporous and Mesoporous Materials in preparation.
[18] H. Miyoshi, H. Matsuo, H. Tanaka, K. Yamada, Y. Oku, S. Takada, N. Hata, T. Kikkawa, Jan. J. Appl. Phys. 44 (2005) 1161–1165.
[19] H. Li, Y. Lin, T.Y. Tsui, J.J. Vlassak, J. Mater. Res. 24 (2009) 107–116.
[20] C. Yacou, M. Fontaine, A. Ayral, P. Lacroix-Desmazes, P. Albouy, A. Julbe, J. Mater. Chem. 18 (2008) 4274–4279.

[21] S. Besson, Films organisés de silice mésoporeuse: synthèse, caractérisation structurale et utilisation pour la croissance de nanoparticules., Ecole Polytechnique, Paris, France, 2002.
[22] Y. Lu, R. Ganguli, C.A. Drewien, M.T. Anderson, C.J. Brinker, W. Gong, Y. Guo, H. Soyez, B. Dunn, M.H. Huang, J.I. Zink, Nature 389 (1997) 364–368.
[23] C. Yacou, Développement de membranes céramiques multifonctionelles à porosité hiérarchique pour le traitement et la séparation de gaz, PhD Thesis, Université Montpellier 2, (2009).
[24] N. Chemin, M. Klotz, V. Rouessac, A. Ayral, E. Barthel, Thin Solid Films 495 (2006) 210–213.
[25] S. Besson, C. Ricolleau, T. Gacoin, C. Jacquiod, J. Boilot, Microporous Mesoporous Mater. 60 (2003) 43–49.
[26] S. Besson, T. Gacoin, C. Jacquiod, C. Ricolleau, D. Babonneau, J. Boilot, J. Mater. Chem. 10 (2000) 1331–1336.
[27] X. Li, B. Bhushan, Mater. Charact. 48 (2002) 11–36.
[28] H.Y. Yu, S.C. Sanday, B.R. Rath, J. Mech. Phys. Solids 38 (1990) 745–764.
[29] C. Hsueh, P. Miranda, J. Mater. Res. 19 (2004) 2774–2781.
[30] J.W. Gardner, V.K. Varadan, O.O. Awadelkarim, Microsensors and smart devices, MEMS, John Wiley & Sons, 2001.
[31] http://www.ceramics.nist.gov/srd/summary/SiO2.htm.
[32] A. Bolshakov, G.M. Pharr, J. Mater. Res. 13 (1998) 1049–1058.
[33] Y. Toivola, A. Stein, F.C. Cook, J. Mater. Res. 19 (2004) 260–271.
[34] D. Tabor, Hardness of Metals, London, Oxford University Press, 1951.
[35] L.J. Gibson, M.F. Ashby, Cellular solids. Structure and properties, second Ed., Cambridge University Press, 1997.
[36] M. Pindera, H. Khatam, A.S. Drago, Y. Bansal, Compos. Part B 40 (2009) 349–378.
[37] Z. Xia, C. Zhou, Q. Yong, X. Wang, Int. J. Solids Struct. 43 (2006) 266–278.
[38] C.L. Martin, R.K. Bordia, Phys. Rev. E 77 (2008) 031307.
[39] A. Delafargue, F. Ulm, Int. J. Solids Struct. 41 (2004) 7351–7360.
[40] X. Chen, Y. Xiang, J.J. Vlassak, J. Mater. Res. 21 (2006) 715–724.
[41] N.A. Fleck, H. Otoyo, A. Needleman, Int. J. Solids Struct. 29 (1992) 1613–1636.
[42] S. Kucheyev, A. Hamza, J. Satcher Jr, M. Worsley, Acta Mater. 57 (2009) 3472–3480.
[43] H. Fan, C. Hartshorn, T. Buchheit, D. Tallant, R. Assink, R. Simpson, D.J. Kissel, D.J. Lacks, S. Torquato, C.J. Brinker, Nat. Mater. 6 (2007) 418–423.